Transition from weak to strong light-molecule coupling: Application to fullerene C_{60} multilayers in metallic cavity

Vito Despoja* and Dino Novko
Institut za fiziku, Bijenička 46, 10000 Zagreb, Croatia
and Donostia International Physics Center (DIPC), P. Manuel de Lardizabal, 4, 20018 San Sebastián, Spain

(Received 6 July 2022; revised 25 October 2022; accepted 26 October 2022; published 1 November 2022)

A common experimental setup to study light-matter interactions consists of semiconducting crystals placed in a metallic cavity that can support confined photons. In that case, the regime of strong coupling can be achieved provided that the semiconducting crystal supports excitons of large oscillatory strength. Here the coupling between transverse-electric cavity-photons and excitons in crystalline C_{60} films of different thicknesses is studied in the framework of the quantum-electrodynamical Bethe-Salpeter equation. The binding strength is characterized by the Rabi splitting Ω of exciton-polaritons as a function of a number of crystal layers N in the van der Waals heterostructures. For the considered nanocavity system a transition from the weak ($\Omega = 50$ meV) to the strong ($\Omega = 350$ meV) coupling with an increasing number of layers N is obtained. This layer-dependent effect seems to be universal, since we also estimate an enhancement of exciton-photon binding energy by a factor of $\sim$4 in hBN multilayers. With this we show that a few nanometer thick two-dimensional heterostructures can significantly modify the zero-point fluctuation energy of cavity photons, which may have many fundamental and practical consequences within the field of light-matter interactions.

DOI: 10.1103/PhysRevB.106.205401

I. INTRODUCTION

Strong coupling between photons and polarization modes at the dielectric interface results in a formation of transverse-magnetic [p(TM)] eigenmodes called surface plasmon-, phonon-, or exciton-polaritons [1–6]. The oscillatory electric field (and thus the current) that they produced is strongly localized at the interface (evanescent field) and parallel to the direction of propagation. As a result, such p(TM) polaritons of the wave vector Q in the nonretarded limit ($Q \gg \omega/c$, where c is the speed of light and ω is the frequency of the field) reduce to longitudinal surface plasmons, phonons, or excitons [3]. On the other hand, the currents supported by the transverse-electric [s(TE)] surface polaritons are perpendicular to the direction of propagation so that these modes are absent in the nonretarded limit, i.e., without the admixture of photons such polarization modes do not survive. Also, due to their evanescent character, these modes behave as "trapped photons."

There are no experimental evidences of the s(TE) surface polaritons at dielectric interfaces, nevertheless, some recent experimental and theoretical investigations indicate that s(TE) exciton-polaritons do exist in two-dimensional (2D) nanostructures [7–13]. Namely, a reduced dimensionality weakens Coulomb screening so that 2D crystals are able to support excitons of large oscillatory strength, which can efficiently couple to photons and form exciton-polaritons [14]. Even though binding between s(TE) photons and excitons in 2D semiconductors, such as single layer transition metal dichalcogenides (TMD), hexagonal boron-nitride (hBN), or phosphorene, is still very weak [12], the coupling can be significantly amplified by increasing the number of crystal layers [13].

Another way to enhance the exciton-photon binding is to spatially confine the photon around the exciton and thus increase the exciton-photon overlap. A very common platform for studying strong light-matter interactions are two-dimensional (2D) semiconducting crystals placed in a planar microcavity [15–22]. Nevertheless, the observed Rabi splittings of about $\Omega \sim 50$ meV between exciton-polariton branches in various TMD microcavity devices [23–29] indicate quite inefficient exciton-photon coupling. However, a remarkable Rabi splitting of about 440 meV is theoretically predicted in the hBN monolayer microcavity [30]. Furthermore, the strongest exciton-photon coupling is achieved in the organic dye molecule thin films placed in a cavity [31]. For instance, the Rabi splitings of $\Omega \leqslant 450$ meV [32–34], 700 meV [35], and even more than 1000 meV [36,37] is detected when various organic dye molecules are placed in planar microcavities.

The theoretical methods dealing with this problem are mostly based on a two-level boson-boson model Hamiltonian with arbitrary coupling constants. In the frequently used Jaynes-Cummings model [38,39] the excitons and photons are described by a two-level Hamiltonian which consists of a lossless cavity mode ω_c and of an exciton ω_s whose binding $\hbar g_s = \mu E\sqrt{\hbar\omega_c/2\epsilon V_c}$ depends on arbitrary parameters; the molecular polarizability μ and cavity electrical field E. In our model, both parameters, the molecular dynamical polarizability [optical conductivity $\sigma(\omega)$] and cavity electrical field propagator $\Gamma(Q, \omega)$, are derived from first principles.

*vito@phy.hr

The generalization of the Jaynes-Cummings model for the case where N identical two-level emitters interact with a cavity mode is known as the Tavis-Cummings model. Even though this model is somewhat closer to the present model of N point molecules, it still implements arbitrary parameters μ and E. Recently, a rigorous quantum-electrodynamical density-functional-theory approach is proposed and applied to molecular exciton-photon coupling, however, in the end, the arbitrary light-matter coupling strength λ is used [40,41]. In Ref. [41] the cavity modeling is simple; the metallic surfaces are assumed to be perfectly reflective and the dielectric substrate is described by a static dielectric constant. Nevertheless, the variable coupling strength is bound by the cavity geometry and manufacturing parameters.

In this paper we investigated the s(TE) exciton-polaritons in crystalline fullerene thin films, i.e., in fcc fullerite cut along (111) planes so that several molecular layers are formed. To achieve the strongest coupling (which occurs in the middle of the cavity), the C_{60} films are additionally deposited at the dielectric Al_2O_3 film whose thickness is approximately half the thickness of the cavity. The exciton-photon coupling is tuned by changing the number of molecular layers N. The light-matter interaction is studied by using our fully microscopic and *ab initio* quantum-electrodynamical Bethe-Salpeter equations (QE-BSE) developed in Refs. [12,30]. In this approach both excitons and photons are described by bosonic propagators σ and Γ, respectively, which are derived from first principles. The C_{60} optical conductivity σ is calculated using the *ab initio* G_0W_0-BSE method [12,42], and the propagator of the free photons Γ is derived by solving the Maxwell's equations at vacuum/dielectric interfaces [43,44]. The exciton-photon coupling is achieved by dressing the free-photon propagator Γ with excitons at the RPA level. We obtain the transition from weak coupling ($\Omega \sim 50$ meV) for $N = 1$ to strong coupling ($\Omega \sim 350$ meV) for $N = 60$. The experimental results of epitaxial growth [45–51] and results of the molecular dynamics simulations of epitaxial growth and stability [51–54] of C_{60} thin films on various substrates show that our model system is highly realistic.

The paper is organized as follows. In Sec. II we present the geometry of the system, the Dyson equation for the photon propagator $\mathcal{E} = \Gamma + \Gamma\tilde{\sigma}\mathcal{E}$, and derivation of the optical conductivity $\tilde{\sigma}$ in the C_{60} monolayer. In Sec. III we present the spectra of electromagnetic modes $S = -\mathrm{Re}\,\mathcal{E}$, the dispersion relations, and intensities of s(TE) exciton-polaritons in a C_{60} thin films microcavity. The conclusions are presented in Sec. IV.

II. THEORETICAL FORMULATION

A. Geometry of the system: Microcavity device

We suppose that the C_{60} thin film is physisorbed at the dielectric substrate of thickness d_2 which is placed in the metallic cavity of thickness $d = d_2 + d_3$. The dielectric response of the substrate's lower and upper metal reflectors are described by the local macroscopic dielectric functions $\epsilon_2(\omega)$, $\epsilon_1(\omega)$, and $\epsilon_4(\omega)$, respectively. The C_{60} thin film is immersed in the dielectric medium of thickness d_3 described by the dielectric constant ϵ_3, as shown in Fig. 1(a). We suppose that

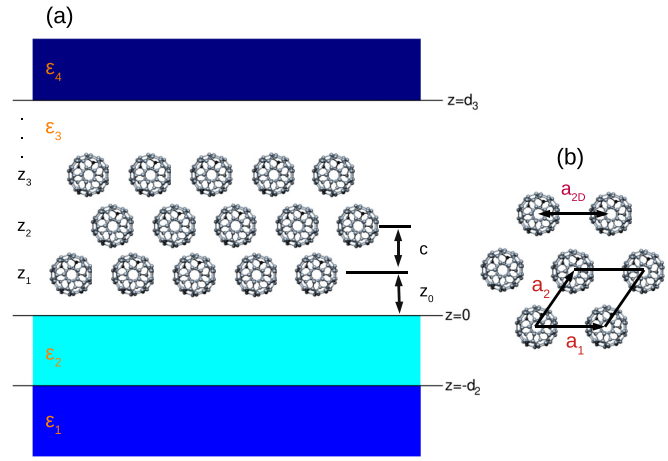

FIG. 1. (a) Geometry of the system. The C_{60} thin film is physisorbed at the dielectric substrate of thickness d_2 which is placed in the metallic cavity of thickness $d = d_2 + d_3$. The C_{60} film is placed in the dielectric medium ϵ_3, and the substrate's lower and upper metal reflectors are described by the dielectric functions $\epsilon_2(\omega)$, $\epsilon_1(\omega)$, and $\epsilon_4(\omega)$, respectively. (b) The molecules C_{60} upon physisorption on the dielectric surface are self-assembled in a regular fcc structure forming the (111) surface. Each crystal plane forms the 2D hexagonal Bravais lattice of the lattice constant $a_{2D} = 9.9$ Å. The separation between layers is $c = 8.1$ Å and the separation between C_{60} and the dielectric surface is $z_0 = 6.5$ Å.

the molecules C_{60} upon physisorbtion on the dielectric surface are self-assembled in a regular fcc structure (the most stable bulk structure of crystalline fullerene) forming the (111) surface. The fcc crystal lattice constant is taken to be $a_{3D} = 14$ Å [54] and the separation between layers is fixed to be $c = a_{3D}/\sqrt{3} = 8.1$ Å. Each crystal plane forms the 2D hexagonal Bravais lattice of the lattice constant $a_{2D} = a_{3D}/\sqrt{2} = 9.9$ Å, as shown in Fig. 1(b). Here the separation between the first C_{60} layer and dielectric surface is chosen to be $z_0 = 6.5$ Å, which corresponds to $z_0 - R_{C_{60}} \sim 3$ Å atom-atom separation, where the C_{60} radius is $R_{C_{60}} \sim 3.5$ Å. The number of molecular crystal monolayers is N.

B. Calculation of electrical field propagator $\mathcal{E}$

The quantity from which we shall extract the information about the electromagnetic modes in C_{60} films placed in a cavity device is electrical field propagator $\mathcal{E}_{\mu\nu}$ which comes from the solution of the Dyson equation [13]

$$\mathcal{E}_{\mu\nu}(\mathbf{r},\mathbf{r}',\omega) = \Gamma_{\mu\nu}(\mathbf{r},\mathbf{r}',\omega) + \sum_{\alpha,\beta=x,y,z}\int d\mathbf{r}_1\int d\mathbf{r}_2\,\Gamma_{\mu\alpha}(\mathbf{r},\mathbf{r}_1,\omega) \times \sigma_{\alpha\beta}(\mathbf{r}_1,\mathbf{r}_2,\omega)\mathcal{E}_{\beta\nu}(\mathbf{r}_2,\mathbf{r}',\omega), \quad (1)$$

where σ represents the nonlocal conductivity tensor in C_{60} film and Γ represents the propagator of the electrical field in the cavity device in the absence of C_{60} film, i.e., when $\sigma = 0$ [12,30]. If each molecule is approximated as a point polarizable dipole, then the optical conductivity of the C_{60}

film can be written as

$$\sigma_{\mu\nu}(\mathbf{r},\mathbf{r}',\omega) = \sum_{i=1}^{N}\sum_{\mathbf{R}_\parallel}\sigma^i_{\mu\nu}(\omega)\delta(\boldsymbol{\rho}-\mathbf{R}_\parallel)\delta(z-z_i)\delta(\boldsymbol{\rho}'-\mathbf{R}_\parallel)\delta(z'-z_i), \tag{2}$$

where $\sigma^i_{\mu\nu}(\omega)$ represents the optical conductivity tensor of a single molecule in the ith molecular layer. Here $\mathbf{r}=(\boldsymbol{\rho},z)$ and $\boldsymbol{\rho}=(x,y)$ are the 3D and 2D position vectors, respectively. This approximation is fully justified in the optical limit when the wavelength is much larger than the dimension of the molecule ($\lambda_{\text{light}} = 2\pi c/\omega_{\text{light}} \gg R_{C_{60}}$). Note that although all molecules are equal, we distinguish their conductivities in different layers σ^i (where $i=1,\ldots,N$) due to the different influence of the substrate on the molecule in different layers. The 2D Bravais lattice translation vectors spanning the molecular crystal are

$$\mathbf{R}_\parallel = n\mathbf{a}_1 + m\mathbf{a}_2; \quad n,m\in\mathbb{Z}, \tag{3}$$

where $\mathbf{a}_1$ and $\mathbf{a}_1$ are the primitive vectors, as illustrated in Fig. 1(b). The molecular layers occupy the planes

$$z_i = z_0, z_0+c, z_0+2c, \ldots, z_0+(N-1)c.$$

If we neglect the electromagnetic field Bragg scattering (on nonphysical point dipoles) at the 2D crystal lattice, the system becomes translationally invariant in the x-y plane and Eq. (1) becomes the tensor equation [13]

$$\mathcal{E}^{ij}_{\mu\nu}(\mathbf{Q},\omega) = \Gamma^{ij}_{\mu\nu}(\mathbf{Q},\omega) + \sum_{\alpha,\beta=x,y,z}\sum_{k=1}^{N}\Gamma^{ik}_{\mu\alpha}(\mathbf{Q},\omega)\tilde{\sigma}^k_{\alpha\beta}(\omega)\mathcal{E}^{kj}_{\beta\nu}(\mathbf{Q},\omega), \tag{4}$$

where $\mathcal{E}^{ij}_{\mu\nu}(\mathbf{Q},\omega)\equiv\mathcal{E}_{\mu\nu}(\mathbf{Q},\omega,z_i,z_j)$ represents the propagator of the electrical field within ($i=j$) or between ($i\neq j$) molecular layers. The optical conductivity of the ith molecular layer is

$$\tilde{\sigma}^i_{\alpha\beta}(\omega) = \frac{1}{S_{\text{fcc}}}\sigma^i_{\alpha\beta}(\omega), \tag{5}$$

where $S_{\text{fcc}} = (\mathbf{a}_1\times\mathbf{a}_2)\hat{\mathbf{z}} = a^2_{2D}\sqrt{3}/2$ is the surface of the 2D unit cell and $\mathbf{Q}=(Q_x,Q_x)$ is the 2D wave vector. The electrical field propagator in the absence of C_{60} film ($\tilde{\sigma}=0$) can be written as [12,13,30]

$$\boldsymbol{\Gamma} = \boldsymbol{\Gamma}^0 + \boldsymbol{\Gamma}^{sc}, \tag{6}$$

where

$$\boldsymbol{\Gamma}^0(\mathbf{Q},\omega,z_i,z_j) = -\frac{4\pi i}{\epsilon_3\omega}\delta(z_i-z_j)\mathbf{z}\cdot\mathbf{z} - \frac{2\pi\omega}{\beta_3 c^2}e^{i\beta_3|z_i-z_j|}\sum_{q=\text{s,p}}\mathbf{e}^0_{\text{q}}\cdot\mathbf{e}^0_{\text{q}} \tag{7}$$

represents the propagator of the "free" electrical field (in the infinite dielectric ϵ_3) and the propagator of the scattered electrical field is [43]

$$\begin{aligned}\boldsymbol{\Gamma}^{sc}(\mathbf{Q},\omega,z_i,z_j) = -\frac{2\pi\omega}{\beta_3 c^2}\sum_{\text{q=s,p}}\frac{1}{D_{3\text{q}}}\big\{&r^-_{\text{q}}e^{i\beta_3(z_i+z_j)}\cdot\mathbf{e}^+_{\text{q}}\cdot\mathbf{e}^-_{\text{q}} \\ &+ r^-_{\text{q}}r^+_{\text{q}}e^{i\beta_3(z_i-z_j+2d_3)}\cdot\mathbf{e}^+_{\text{q}}\cdot\mathbf{e}^+_{\text{q}} \\ &+ r^+_{\text{q}}e^{-i\beta_3(z_i+z_j-2d_3)}\cdot\mathbf{e}^-_{\text{q}}\cdot\mathbf{e}^+_{\text{q}} \\ &+ r^-_{\text{q}}r^+_{\text{q}}e^{-i\beta_3(z_i-z_j-2d_3)}\cdot\mathbf{e}^-_{\text{q}}\cdot\mathbf{e}^-_{\text{q}}\big\}.\end{aligned}$$

Here $D_{3\text{q}} = 1 - r^-_{\text{q}}r^+_{\text{q}}e^{2i\beta_3 d_3}$ and the unit vectors of s(TE) and p(TM) polarized electromagnetic fields are

$$\mathbf{e}^{0,\pm}_s = \mathbf{Q}_0\times\mathbf{z}$$

and

$$\mathbf{e}^{0,\pm}_p = \frac{c}{\omega\sqrt{\epsilon_3}}[\alpha_{0,\pm}\beta_3\mathbf{Q}_0 + Q\mathbf{z}],$$

respectively. Here $\alpha_0 = -\text{sgn}(z_i-z_j)$, $\alpha_\pm = \mp 1$, and $\mathbf{Q}_0$ and $\mathbf{z}$ are unit vectors in $\mathbf{Q}$ and z directions, respectively. The reflection coefficients at ϵ_3/ϵ_2 and ϵ_3/ϵ_4 interfaces are

$$r^-_{\text{q}} = \frac{1}{D_{2\text{q}}}\{r_{3/2\text{q}} + r_{2/1\text{q}}e^{2i\beta_2 d_2}\} \tag{8}$$

and

$$r^+_{\text{q}} = r_{3/4\text{q}}, \tag{9}$$

respectively, where $D_{2\text{q}} = 1 - r_{2/1\text{q}}r_{2/3\text{q}}e^{2i\beta_2 d_2}$. The reflection coefficients of s and p polarizations at single interface ϵ_i/ϵ_j are

$$r_{i/js} = \frac{\beta_i-\beta_j}{\beta_i+\beta_j}$$

and

$$r_{i/jp} = \frac{\beta_i\epsilon_j - \beta_j\epsilon_i}{\beta_i\epsilon_j + \beta_j\epsilon_i}.$$

The complex wave vectors in a perpendicular (z) direction are

$$\beta_i = \sqrt{\frac{\omega^2}{c^2}\epsilon_i(\omega) - |\mathbf{Q}|^2}; \quad i=1,\ldots,4. \tag{10}$$

The β_i determines the character of the electromagnetic modes in the ith dielectric.

Here we assume that the two metallic reflectors are made of aluminum (Al) and the substrate is alumina (Al_2O_3) so that $\epsilon_1=\epsilon_4=\epsilon_{\text{Al}}(\omega)$ and $\epsilon_2=\epsilon_{\text{Al}_2\text{O}_3}(\omega)$, where $\epsilon_{\text{Al}}(\omega)$ and $\epsilon_{\text{Al}_2\text{O}_3}(\omega)$ are local macroscopic dielectric functions derived from first principles as in Ref. [65]. The dielectric medium is vacuum, i.e., $\epsilon_3=1$. Aluminum is approximately a Drude metal supporting bulk plasmon at $\omega_p\approx 15$ eV so that $\text{Re}\,\epsilon_{\text{Al}}(\omega<\omega_p)<0$ and $\text{Im}\,\epsilon_{\text{Al}}(\omega<\omega_p)\approx 0$. As a result, the $\beta_{1,4}$ are imaginary numbers and the electromagnetic field has an evanescent character inside the metal for $\omega<\omega_p$. Because C_{60} excitons are far below ω_p, the Al walls behave as perfect reflectors. The $\text{Re}\,\epsilon_{\text{Al}_2\text{O}_3}$ is almost constant ($\text{Re}\,\epsilon_{\text{Al}_2\text{O}_3}\approx 3$) in the IR and in the visible range ($\omega<3$ eV) while $\text{Im}\,\epsilon_{\text{Al}_2\text{O}_3}\approx 0$ up to the band gap energy ($E_g\sim 6$ eV). Therefore, Al_2O_3 is a good choice for the substrate since its electronic excitations are mostly above the C_{60} excitons.

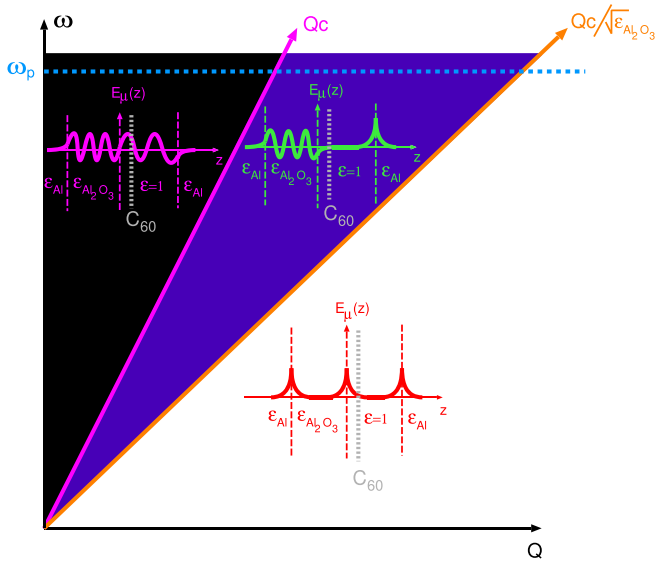

FIG. 2. (a) The character of the electromagnetic modes in the Al/Al_2O_3/vacuum/Al cavity. In the region $\omega > Qc$ the electromagnetic modes are entirely radiative (both in vacuum and in the substrate), in the region $Qc/\sqrt{\epsilon_{Al_2O_3}} < \omega < Qc$ they are radiative in the dielectric and evanescent in the vacuum, and in $\omega < Qc/\sqrt{\epsilon_{Al_2O_3}}$ region they have fully evanescent character. Below the plasmon frequency ω_p the metal walls are perfectly reflective.

In the vacuum, for $\omega > Qc$, the β_3 is a real number so that electromagnetic modes have radiative character, and for $\omega < Qc$, the β_3 is an imaginary number so that the electromagnetic modes have evanescent character. These two regions are separated by the so-called "light-line" $\omega = Qc$, as illustrated by the magenta line in Fig. 2. In the Al_2O_3 substrate the evanescent and radiative regions are separated by the $\omega = Qc/\sqrt{\epsilon_{Al_2O_3}(\omega)}$ line, as illustrated by the orange line in Fig. 2. Since $\mathrm{Re}\,\epsilon_{Al_2O_3}(\omega < E_g) > 1$, the slope of the light line in the substrate is smaller than in the vacuum so that in the gap $Qc/\sqrt{\epsilon_{Al_2O_3}} < \omega < Qc$ the light propagates freely into the substrate, but has an evanescent character in the vacuum region. Therefore, if the exciton-polariton is excited in the region $\omega > Qc$, it is a fully radiative mode spreading within the metallic cavity $-d_2 < z < d_3$, and if it is excited in the region $Qc/\sqrt{\epsilon_{Al_2O_3}} < \omega < Qc$, it has an evanescent character but it also can hybridize with a radiative mode confined in the substrate $(-d_2 < z < 0)$ forming a surface-polariton resonance. These modes shall be referred to as vacuum-evanescent/substrate-radiative modes. Finally, if the exciton-polariton is excited in the region $\omega < Qc/\sqrt{\epsilon_{Al_2O_3}}$, it has a fully evanescent character.

In order to better understand the impact of the cavity geometry on the interplay between the excitons and cavity photons, here we shall briefly analyze the intensity of electromagnetic modes in the empty cavity, i.e., when $\sigma = 0$. Figure 3 shows the spectral intensities $S(Q_y, \omega)$ of the s(TE) cavity modes $n = 1, 2, \ldots$ in the Al/Al_2O_3/vacuum/Al cavity of thicknesses (a) $d_2 = 0$, $d_3 = 200$ nm, (b) $d_2 = 50$ nm, $d_3 = 150$ nm, (c) $d_2 = 100$ nm, $d_3 = 100$ nm, and (d) $d_2 = 150$ nm, $d_3 = 50$ nm. Note that the thickness of the metallic cavity is kept constant, i.e., $d = d_2 + d_3 = 200$ nm. In the absence of the substrate $(d_2 = 0)$ the cavity (in the shown energy interval) supports two well-defined cavity photons $n = 1$ and $n = 2$, situated in the radiative region $\omega > Qc$. When thin substrate $(d_2 = 50$ nm) is introduced, the cavity mode $n = 1$ is weak, while the mode $n = 2$ is significantly redshifted so that they become closer. For $\omega > E_g$ the cavity modes $n = 1, 2$ decay due to the interband electron-hole excitations in Al_2O_3. One can also see the diffusive cavity mode $n = 3$, completely immersed in the interband electron-hole continuum. A significant part of the mode $n = 1$ is vacuum-evanescent/substrate-radiative, while modes $n = 2, 3$ are mostly fully radiative. For the thicker substrate $(d_2 = 100$ nm) modes $n = 1$ and 2 bend towards the light line $\omega = Qc/\sqrt{\epsilon_{Al_2O_3}}$, while the mode $n = 3$ is lowered below E_g. However, due to strong substrate screening for $\omega \approx E_g$, it loses its intensity. For the thick substrate $(d_2 = 150$ nm) the cavity photons $n = 1, 2, 3$ are additionally redshifted below E_g, behaving as well-defined electromagnetic eigenmodes. Our goal here is to use the cavity setup so that the principal photon $n = 1$ is just starting to cross the exciton ω_{ex1} in order to achieve a stronger binding. Considering that the principal photon $n = 1$ is here at $\hbar\omega_{n=1} \sim 2$ eV this will be apparently achieved for a somewhat thinner cavity.

C. Calculation of the optical conductivity $\tilde{\sigma}$

In order to determine the single molecule optical conductivity $\sigma(\omega)$, we first calculate the KS states $|\phi_n\rangle$ of an isolated molecule. Considering that we use the plane-wave DFT code (the system is periodic) the Bravais lattice and a unit cell

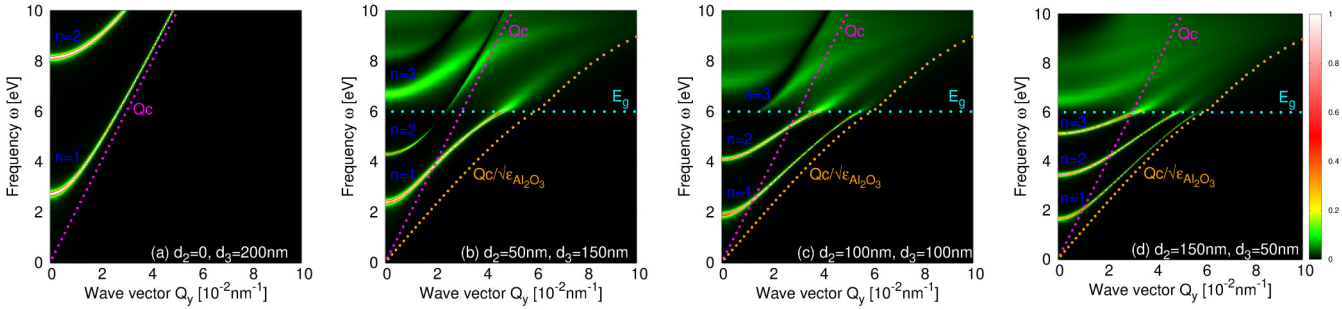

FIG. 3. (a) The spectral intensity $S(Q_y, \omega)$ of the s(TE) cavity modes $n = 1, 2, 3$ in the empty $(\sigma = 0)$ Al/Al_2O_3/vacuum/Al cavity of thicknesses: (a) $(d_2 = 0, d_3 = 200$ nm; (b) $d_2 = 50$ nm, $d_3 = 150$ nm; (c) $d_2 = 100$ nm, $d_3 = 100$ nm, and (d) $d_2 = 150$ nm, $d_3 = 50$ nm. Note that the thickness of the metallic cavity is kept constant $d = d_2 + d_3 = 200$ nm.

a are chosen so that the neighboring molecular orbitals do not overlap. It should be emphasized here that the Bravais lattice and unit cell a should not be related to the previously described fcc lattice of the unit cell a_{3D}. Here we assume that molecules are periodically repeating so that they form a simple-cubic (sc) Bravais lattice with unit cell parameter a and volume $\Omega_{sc} = a^3$. The molecular states $|\phi_n\rangle$ are calculated at the Γ point only [center of the Brillouin zone (BZ)]. The nonlocal optical conductivity tensor of a single molecule in the ith layer is [13,42]

$$\sigma^i_{\mu\nu}(\mathbf{r},\mathbf{r}',\omega) = \frac{2i}{\omega}\sum_{nm}\sum_{n'm'}\mathcal{K}^{m\leftarrow m',i}_{n\rightarrow n'}(\omega) j^{\mu}_{nm}(\mathbf{r})[j^{\nu}_{n'm'}(\mathbf{r}')]^*, \tag{11}$$

where

$$j^{\alpha}_{nm}(\mathbf{r}) = \frac{e\hbar}{2im}\{\phi^*_n(\mathbf{r})\partial_\alpha\phi_m(\mathbf{r}) - [\partial_\alpha\phi^*_n(\mathbf{r})]\phi_m(\mathbf{r})\} \tag{12}$$

represents the current produced by transitions between molecular states $|\phi_n\rangle \rightarrow |\phi_m\rangle$. Considering that the Bloch wave functions in the Γ point ϕ_n are periodic functions, tensor Eq. (11) can be expanded in the Fourier series

$$\sigma^i_{\mu\nu}(\mathbf{r},\mathbf{r}',\omega) = \frac{1}{\Omega_{sc}}\sum_{\mathbf{G}\mathbf{G}'} e^{i\mathbf{G}\mathbf{r}}e^{-i\mathbf{G}'\mathbf{r}'}\sigma^{\mu\nu,i}_{\mathbf{G}\mathbf{G}'}(\omega), \tag{13}$$

where the Fourier coefficients are

$$\sigma^{\mu\nu,i}_{\mathbf{G}\mathbf{G}'}(\omega) = \frac{i}{\omega}\frac{2}{\Omega_{sc}}\sum_{nm}\sum_{n'm'} j^{\mu}_{nm}(\mathbf{G})\mathcal{K}^{m\leftarrow m',i}_{n\rightarrow n'}(\omega)[j^{\nu}_{n'm'}(\mathbf{G}')]^*, \tag{14}$$

and where the current vertices are

$$j^{\alpha}_{nm}(\mathbf{G}) = \int_{\Omega_{sc}} d\mathbf{r} e^{-i\mathbf{G}\mathbf{r}}\, j^{\alpha}_{nm}(\mathbf{r}). \tag{15}$$

The four-point polarizability $\mathcal{K}^i$ can be obtained by solving the Bethe-Salpeter equation [12,30]

$$\mathcal{K}^{m\leftarrow m',i}_{n\rightarrow n'}(\omega) = \mathcal{L}^{m\leftarrow m',i}_{n\rightarrow n'}(\omega) + \sum_{n_1m_1}\sum_{n_2m_2}\mathcal{L}^{m\leftarrow m_1,i}_{n\rightarrow n_1}(\omega)\,\Xi^{m_1\leftarrow m_2,i}_{n_1\rightarrow n_2}\,\mathcal{K}^{m_2\leftarrow m',i}_{n_2\rightarrow n'}(\omega). \tag{16}$$

The time-ordered electron-hole propagator is

$$\mathcal{L}^{m\leftarrow m',i}_{n\rightarrow n'}(\omega) = \frac{f^i_n - f^i_m}{\omega + E^i_n - E^i_m + i\delta\mathrm{sgn}\left(E^i_m - E^i_n\right)}\delta_{nn'}\delta_{mm'}, \tag{17}$$

where $f^i_n = \theta(E^i_F - E^i_n)$ are Fermi-Dirac distributions at $T = 0$. The molecular eigenenergies E^i_n are calculated using the quasiparticle G_0W^i method which includes the Al_2O_3 substrate polarization effects [13]. The Bethe-Salpeter kernel is

$$\Xi^{m\leftarrow m',i}_{n\rightarrow n'} = \Xi^{H,m\leftarrow m',i}_{n\rightarrow n'} - \tfrac{1}{2}\Xi^{F,m\leftarrow m',i}_{n\rightarrow n'}, \tag{18}$$

where the BS-Hartree kernel is

$$\Xi^{H,m\leftarrow m',i}_{n\rightarrow n'} = \frac{1}{\Omega_{sc}}\sum_{\mathbf{G}_1\mathbf{G}_2}\rho^*_{nm}(\mathbf{G}_1)\,V^{C,i}_{\mathbf{G}_1\mathbf{G}_2}\rho_{n'm'}(\mathbf{G}_2), \tag{19}$$

and the BS-Fock kernel is

$$\Xi^{F,m\leftarrow m',i}_{n\rightarrow n'} = \frac{1}{\Omega_{sc}}\sum_{\mathbf{G}_1\mathbf{G}_2}\rho^*_{nn'}(\mathbf{G}_1)W^i_{\mathbf{G}_1\mathbf{G}_2}(\omega=0)\rho_{mm'}(\mathbf{G}_2). \tag{20}$$

The "time-ordered" screened Coulomb potential in the ith molecular layer (including the polarization of the Al_2O_3 surface) is the solution of the Dyson's equation

$$W^i_{\mathbf{G}\mathbf{G}'}(\omega) = V^{C,i}_{\mathbf{G}\mathbf{G}'} + \sum_{\mathbf{G}_1\mathbf{G}_2}V^{C,i}_{\mathbf{G}\mathbf{G}_1}\chi^0_{\mathbf{G}_1\mathbf{G}_2}(\omega)W^i_{\mathbf{G}_2\mathbf{G}'}(\omega), \tag{21}$$

where the matrix of the time-ordered irreducible polarizability is

$$\chi^0_{\mathbf{G}\mathbf{G}'}(\omega) = \frac{2}{\Omega_{sc}}\sum_{nm}\frac{(f_n - f_m)\rho_{nm}(\mathbf{G})\,\rho^*_{nm}(\mathbf{G}')}{\hbar\omega + E_n - E_m + i\delta\mathrm{sgn}(E_m - E_n)}, \tag{22}$$

and the charge vertices are

$$\rho_{nm}(\mathbf{G}) = \int_{\Omega_{sc}} d\mathbf{r}\,\phi^*_n(\mathbf{r})e^{-i\mathbf{G}\mathbf{r}}\phi_m(\mathbf{r}). \tag{23}$$

The molecular eigenenergies E_n in Eq. (22) are bare Kohn-Sham energies without quasiparticle corrections. The Coulomb potential that propagates interactions in the ith molecular layer, excluding the polarization of the molecular layer (i.e., when $\chi^0 = 0$), is [13]

$$V^{C,i}_{\mathbf{G}_1\mathbf{G}_2} = V^{C}_{\mathbf{G}_1\mathbf{G}_2} + \Delta V^{S,i}_{\mathbf{G}_1\mathbf{G}_2}(\omega).$$

The bare truncated Coulomb potential is

$$V^{C}_{\mathbf{G}\mathbf{G}'} = \frac{4\pi}{|\mathbf{G}|^2}[1 - \cos(|\mathbf{G}|R_C)]\delta_{\mathbf{G}\mathbf{G}'}, \tag{24}$$

where R_C, the range of the potential, prevents the spurious interaction with surrounding molecules in the sc lattice [55]. The induced Coulomb potential

$$\Delta V^{S,i}_{\mathbf{G}\mathbf{G}'}(\omega) = \frac{D(\omega)}{\Omega_{sc}}\int\frac{d\mathbf{Q}}{(2\pi)^2}v_Q e^{-2Qz_i}F_{\mathbf{G}}(\mathbf{Q})F^*_{\mathbf{G}'}(\mathbf{Q}) \tag{25}$$

represents the polarization of the Al_2O_3 surface [13,42]. Here $v_Q = \frac{2\pi}{|\mathbf{Q}|}$ and $D(\omega) = [1 - \epsilon_{Al_2O_3}(\omega)]/[1 + \epsilon_{Al_2O_3}(\omega)]$. The form factors are

$$F_{\mathbf{G}}(\mathbf{Q}) = 8(-1)^{n_z}\frac{\sin\left[(Q_x - G_x)\frac{a}{2}\right]\sin[(Q_y - G_y)\frac{a}{2}]\sinh\left[Q\frac{a}{2}\right]}{(Q_x - G_x)(Q_y - G_y)(Q + iG_z)}, \tag{26}$$

where the reciprocal vectors of the sc lattice are $\mathbf{G} = (G_x, G_y, G_z) = \frac{2\pi}{a}(n_x, n_y, n_z)$ and $n_x, n_y, n_z \in \mathbb{Z}$. Finally, considering that the interaction $V^{C,i}$ prevents the correlations between conductivities in adjacent cells, the conductivity of an isolated molecule is equal to the conductivity per unit cell

$$\sigma^i_{\mu\nu}(\omega) = \int_{\Omega_{sc}} d\mathbf{r}\int_{\Omega_{sc}} d\mathbf{r}'\sigma^i_{\mu\nu}(\mathbf{r},\mathbf{r}',\omega). \tag{27}$$

After combining Eqs. (13) and (27), the optical conductivity of single molecule becomes

$$\sigma^i_{\mu\nu}(\omega) = \Omega_{sc}\sigma^{\mu\nu,i}_{\mathbf{G}=0\mathbf{G}'=0}(\omega). \tag{28}$$

By employing Eqs. (5), (14), and (28) we determine the explicit expression for the surface optical conductivity

$$\tilde{\sigma}^{i}_{\mu\nu}(\omega) = \frac{2i}{\omega S_{\rm fcc}} \sum_{nm} \sum_{n'm'} j^{\mu}_{nm}(\mathbf{G}=0) \mathcal{K}^{m\leftarrow m',i}_{n\rightarrow n'}(\omega) [j^{\nu}_{n'm'}(\mathbf{G}'=0)]^{*}, \tag{29}$$

which enters in the Dyson's equation for an electrical field propagator (4). Note that the dimension of conductivity (29) is exactly the quantum of conductance $G_0 = \frac{2\pi e^2}{h}$, an already standardized unit for describing the optical conductivity in 2D crystals [12,30,56]. Accordingly, the $\tilde{\sigma}^{i}_{\mu\nu}(\omega)$ represents the optical conductivity of the ith molecular layer.

In the above approach the single C_{60} layer behaves as a homogeneous polarizable 2D sheet in which response is described by the local conductivity Eq. (29). Further improvements of $\tilde{\sigma}$ would be retained of its spatial dispersivity or inclusion of the crystal local field effect ($\mathbf{G}, \mathbf{G}' \neq 0$). However, these effects are negligible in the optical limit ($2\pi/\beta_3 \gg a$). So the only serious approximation we use here is actually neglecting the (intra- and interlayer) molecular overlap, i.e., we assume that the crystalline fullerite band structure is dispersionless.

Finally it should be emphasized here that the retardation effects are not included in the calculation of molecular conductivity (28). This is because we approximate that the interaction between charge or current fluctuations within one molecule is mediated only by longitudinal photons, i.e., only by instantaneous Coulomb interactions V and $W(\omega = 0)$, appearing in the BSE Hartree (19) and Fock (20) kernels, respectively. This approximation is (up to superfine structure corrections) completely justified. Namely, if the frequency of the electronic mode is ω, then $\omega/c \ll a$ (or $c \gg \omega/a$), i.e., a transversal photon during one period $1/\omega$ passes a distance that is incomparably larger than the unit cell a, so that interactions within a molecule can be freely approximated as instantaneous. However, the intermolecular interactions, between molecules which extend over a macroscopic cavity (when $c \sim \omega/d$), are mediated both by longitudinal and transversal photons. Both interactions are simultaneously implemented in the photon propagators Γ and $\mathcal{E}$ which in the nonretarded limit ($c \to \infty$) reduce to longitudinal interactions V and W. So, the light-matter interaction is here included only at the RPA stage through the Dyson equation (4) and we think that this is a good enough approximation regardless of the light-matter binding strength. This point is also stressed in our recent publication [12].

D. Computational details

The fullerene KS orbitals $\phi_n(\mathbf{r})$ and energies E_n are calculated using the plane-wave self-consistent field DFT code (PWSCF) within the QUANTUM ESPRESSO (QE) package [57]. The core-electrons interaction is approximated by the norm-conserving pseudopotentials [58,59] so that the number of occupied valence states is 120. The exchange correlation (XC) potential is approximated by the Perdew-Burke-Ernzerhof (PBE) generalized gradient approximation (GGA) functional [60]. The plane-wave cut-off energy is 60 Ry. The molecules are arranged in the simple-cubic Bravais lattice of unit cell $a = 18$ Å with one molecule per unit cell. Since there is no intermolecular overlap, the ground state electronic density is calculated at the Γ point only. The geometries have been fully relaxed, with all forces $\lesssim$0.02 eV/Å. The RPA time-ordered screened Coulomb interaction W^i (21) is calculated using the energy cutoff of 2 Ry (∼27 eV) and the bands summations (n, m) in the irreducible polarizability (22) are performed using 240 molecular states. The G_0W^i calculation of the fullerene C_{60} eigenenergies E^i_n is described in detail in Ref. [13]. The bare BS-Hartree-Fock kernels, Eqs. (19) and (20) that are derived using bare interaction $V^{\rm C}$, are calculated using the energy cutoff of 8 Ry (∼109 eV), and induced BS-Hartree-Fock kernels, Eqs. (19) and (20) that are derived using induced interactions $\Delta V^{{\rm S},i}$ and $W^i - V^{\rm C}$, respectively, are calculated using the energy cutoff of 2 Ry (∼27 eV). During the evaluation of BSE-HF kernels we used 42 occupied (HOMO-41,...,HOMO) and 42 unoccupied (LUMO,...,LUMO+41) molecular states. In order to achieve the accurate (experimental) exciton energy the calculation is provided beyond the Tamm-Dancoff approximation, i.e., the dimension of the BSE-HF kernel matrix is $2 \times 42 \times 42 = 3528$. The damping parameters δ used in Eqs. (17) and (22) are 50 and 200 meV, respectively. For the radial cutoff in truncated interaction (24), we use $R_{\rm C} = a/2 = 9$ Å. The integration in Eq. (25) is performed over two-dimensional wave vectors $\mathbf{Q} = (Q_x, Q_x)$ using a 121×121 rectangular mesh and the cutoff wave vector $Q_{\rm C} = 0.5$ a.u.

III. RESULTS AND DISCUSSION

First we determine the QP and optical properties of isolated (gas-phase) C_{60} molecules. The calculated G_0W_0 HOMO-LUMO gap is $E_g = 4.66$ eV which agrees very well with the experimental value of about 5 eV [61–64]. When the molecular layer is deposited on the Al_2O_3 surface, the gap reduces to $E_g = 4.26$ eV. Here the separation is chosen to be $z_0 = 6.5$ Å. Just for comparison we also determine the HOMO-LUMO gap when C_{60} is deposited on the silver (Ag) surface, which is described also in terms of the *ab initio* macroscopic dielectric function [65]. For the same separation z_0 the gap on Ag is $E_g = 3.81$ eV, which corresponds to a twofold energy gap reduction as compared to the insulator surface. The image-theory estimation of the HOMO-LUMO gap at a metallic surface would be $E_g \sim 3.56$ eV which, as expected, overestimates the G_0W_0 result. Figure 4 shows calculated G_0W_0-BSE optical conductivities $\tilde{\sigma}_{xx}(\omega)$ in the self-standing molecular layer (black solid line) and in the molecular layer deposited on the Al_2O_3 dielectric surface (cyan dashed line), where $z_0 =$ 6.5 Å. For comparison, the experimental optical absorbtion in fullerene C_{60} is shown by red circles [66]. This experimental study, along with others [67,68], show three broad excitation bands at $\omega_{\rm ex1} \sim 3.9$ eV, $\omega_{\rm ex2} \sim 4.9$ eV, and $\omega_{\rm ex3} \sim 6$ eV, which agrees very well with our results. It should be emphasized here that, because the band gap is $E_g = 4.66$ eV, only the excitation band $\omega_{\rm ex1}$ can be considered as exciton by definition, whose binding energy is $E_g - \hbar\omega_{\rm ex1} \sim 0.76$ eV. In fact, the strong maximum $\omega_{\rm ex3}$ is usually referred to as the π plasmon [69,70]. All three excitons are the result of electronic transitions within the C_{60} π complex. When the molecule

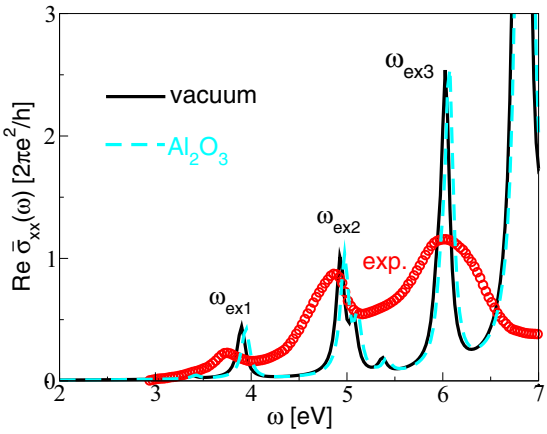

FIG. 4. The optical conductivities $\tilde{\sigma}_{xx}(\omega)$ of the C_{60} monolayer in vacuum (black solid line), on the Al_2O_3 dielectric surface (cyan dashed line), and the experimental optical absorbtion of C_{60} in the gas phase [66] (red circles).

is deposited at the Al_2O_3 surface, the excitation bands are almost unaltered. The latter comes from the substrate-induced weakening of the interaction between the excited electron and hole which in turn reduces the exciton binding energy and thus cancel the gap reduction [42,71,72]. Since the dielectric surface weakly influences the molecular optical conductivity, we shall assume that $\tilde{\sigma}^{i}_{xx}(\omega)$ does not depend on i and is equal to the optical conductivity in the self-standing molecular layer. This means that the impact of the dielectric substrate on the electromagnetic modes in the C_{60} films is reduced to the propagator Γ^{sc}, which enters the Dyson's equation (4).

The electromagnetic modes are explored in the $Al/Al_2O_3/vacuum/Al$ cavity of thickness $d = d_2 + d_3 = 90$ nm, where we chose $d_2 = 40$ nm and $d_3 = 50$ nm. These parameters are chosen so that the cavity supports just one (principal $n = 1$) cavity photon which barely intersects the exciton ω_{ex1}. In the following we focus on the spectral intensity of the s(TE) polarized electromagnetic modes. Moreover, we explore the s(TE) modes propagating in the y direction ($\mathbf{Q} = Q_y\mathbf{y}$) so that the tensor $\mathcal{E}$ has only one $(\mu\nu)$ component $\mathcal{E}^{ij}_{xx}$. The spectra of the s(TE) electromagnetic modes in the C_{60} films will be mostly analyzed using the real part of the propagator $\mathcal{E}$ in the topmost molecular layer $(ij = NN)$:

$$S(Q_y, \omega) = -\mathrm{Re}\,\mathcal{E}^{NN}_{xx}(Q_y\mathbf{y}, \omega). \tag{30}$$

Figure 5(a) shows the spectral intensity of the s(TE) polarized electromagnetic modes $S(Q_y, \omega)$ in the empty $Al/Al_2O_3/vacuum/Al$ cavity, without the C_{60} film ($N = 0$). For $Q_y = 0$ it has energy $\omega_{n=1} = 3.8$ eV, slightly below ω_{ex1}, and approximately at 5 eV, when it intersects ω_{ex2}, it enters the region $Qc/\sqrt{\epsilon_{Al_2O_3}} < \omega < Qc$ when it becomes a

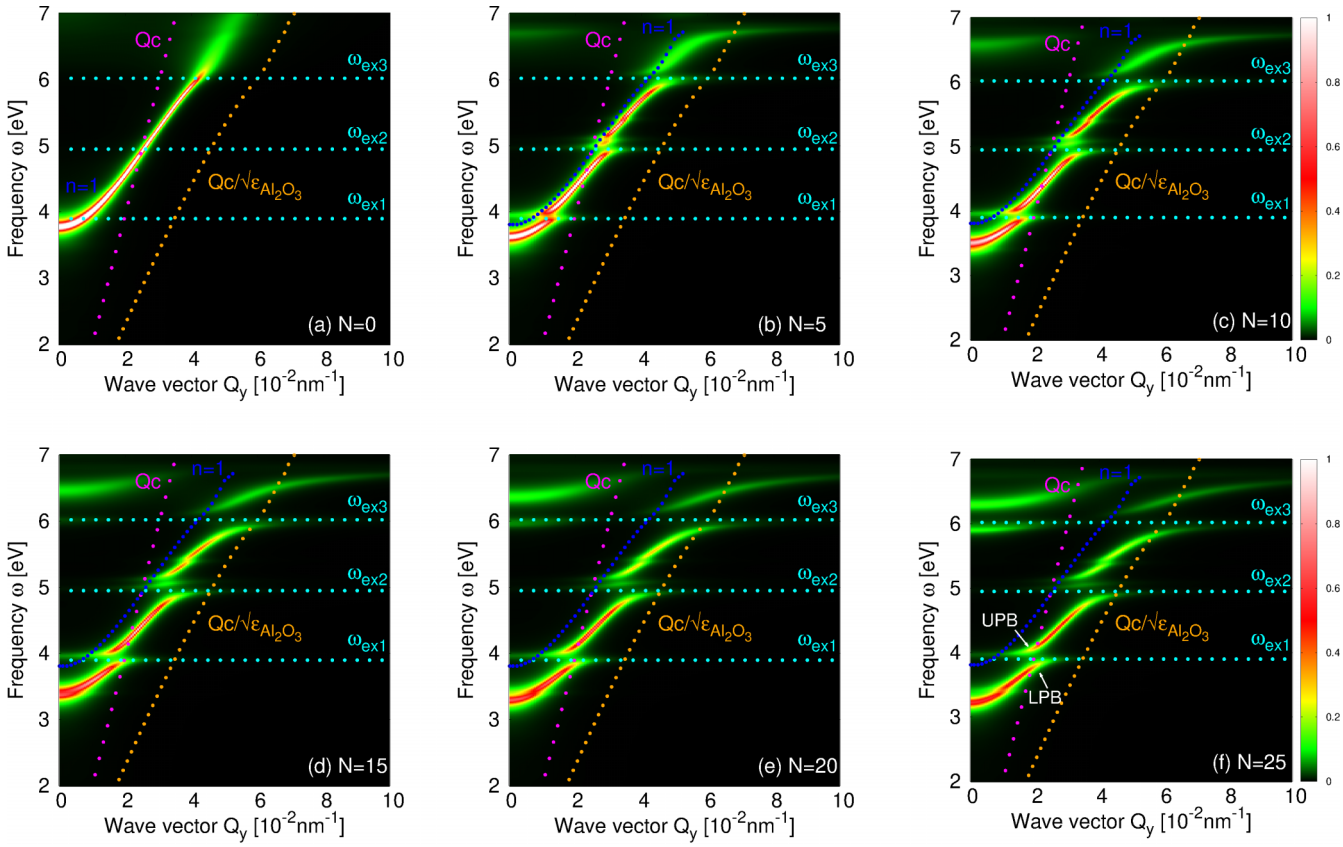

FIG. 5. (a) The spectral intensity $S(Q_y, \omega)$ of the s(TE) cavity mode $n = 1$ in the empty cavity (a) $N = 0$, and in the cavity supporting C_{60} film of thicknesses (b) $N = 5$, (c) $N = 10$, (d) $N = 15$, (e) $N = 20$, and (f) $N = 25$. The $Al/Al_2O_3/vacuum/Al$ cavity parameters are $d_2 = 40$ nm and $d_3 = 50$ nm.

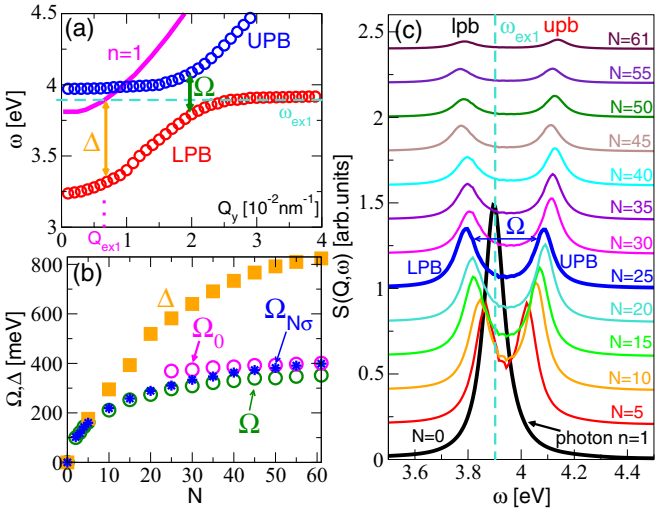

FIG. 6. (a) The exciton-polariton branches LPB and UPB, Rabi splitting Ω, and photon shift Δ resulting from the hybridization between the cavity photon $n = 1$ and exciton ω_{ex1} in the C_{60} thin film of thickness $N = 25$. (b) The Rabi splitting Ω (green circles) and the photon shift Δ (orange squares) as a function of the number of C_{60} layers N. Blue stars denote the Rabi splitting $\Omega_{N\sigma}$ in single C_{60} layer whose optical conductivity scales as $N\tilde{\sigma}(\omega)$. The Rabi splitting in the absence of Al_2O_3 substrate Ω_0 is denoted by the magenta circles. (c) The spectral intensity of the s(TE) electromagnetic modes in the C_{60} films of various thicknesses, $N = 5, 10, \ldots, 61$, close to the avoided crossing. The $N = 0$ shows the intensity of the unperturbed photon $n = 1$.

vacuum-evanescent/substrate-radiative mode (see Fig. 2). For $\omega > E_g \sim 6$ eV the cavity photon decays into the incoherent electron-hole excitations in Al_2O_3. In the case where the Al_2O_3 slab would be removed, the cavity photon would be blueshifted from 3.8 to 5.3 eV, which in turn would disable crossing with the excitons ω_{ex1} and ω_{ex2}. According to the simplified formula for $n = 1$ photon energy [30]

$$\omega_{n=1}(Q = 0) = c\pi/d,$$

the exciton-cavity photon crossing could be achieved by increasing the cavity thickness d. Increasing the thickness d would reduce the exciton-photon overlap and thus weaken their hybridization. However, even though the inclusion of the substrate induces the photon redshift (as demonstrated in Fig. 3), which makes the exciton-photon crossing occur at smaller d (when the spatial exciton-photon overlap is larger), this positive effect is canceled by the dielectric-induced reduction of the photon intensity. Therefore, the exciton-photon binding should not be significantly affected by the substrate. We shall show later, in Fig. 6, that this is indeed the case.

Figures 5(b)–5(f) show the spectral intensity of the s(TE) modes in C_{60} thin films of thicknesses $N = 5$, 10, 15, 20, and 25, respectively. The blue dotted line represents the unperturbed ($N = 0$) cavity photon $n = 1$. For $N = 5$ and 10 all three excitons are visibly intersecting the cavity photons, where for $N = 10$ the avoided crossings can clearly be observed. For $N = 15$, 20, and 25 a significant splitting appears in the photon dispersion, which means that a strong exciton-photon binding is achieved and the exciton-polaritons are formed. The splitting is larger at the intersection with higher excitons ω_{ex2} and ω_{ex3} due to their larger oscillatory strengths (see Fig. 4). The lower and upper exciton-polariton branches are abbreviated as LPB and UPB, respectively [also denoted in Fig. 5(f)]. Note that the exciton-polaritons resulting from hybridization with ω_{ex2} and ω_{ex3} are mostly in the region $Qc/\sqrt{\epsilon_{Al_2O_3}} < \omega < Qc$. So they are surface-polariton resonances, i.e., the evanescent modes through the C_{60} slab, which hybridize with the cavity modes confined in the substrate ($-d_2 < z < 0$). The exciton-polaritons originating from ω_{ex1} are mostly in the region $\omega > Qc$, so they have radiative character through the entire metallic cavity ($-d_2 < z < d_3$). These radiative exciton-polaritons are fundamentally the most interesting, so we shall focus on them.

Figures 5(d)–5(f) clearly show how photons do not change only at the intersection points, but they also change their global shape. For example, when compared with the unperturbed photon dispersion (blue dots), the significant redshift is noticeable. This is because the thicker layer behaves as a dielectric adlayer which (similar to the dielectric Al_2O_3 substrate) redshifts the photon dispersion. The latter is a classical electrodynamic effect with no big fundamental significance. True hybrid exciton-polariton modes arise at (and closely around) the point where the exciton intersects the redshifted photon. The dispersions at the far left and far right of that area correspond to the pure exciton or photon. Therefore, here we define the Rabi splitting as the minimum energy difference between the UPB and LPB, which are results of the hybridization of the cavity photon $n = 1$ and the exciton ω_{ex1} [see Fig. 6(a)],

$$\Omega = \min\{\omega_{UPB}(Q) - \omega_{LPB}(Q)\}. \tag{31}$$

The photon shift is defined as the difference between the exciton ω_{ex1} and LPB at the crossing wave vector Q_{ex1},

$$\Delta = \omega_{ex1} - \omega_{LPB}(Q_{ex1}). \tag{32}$$

The crossing wave vector is defined as $\omega_{n=1}(Q_{ex1}) = \omega_{ex1}$, where $\omega_{n=1}(Q)$ represents the dispersion relation of unperturbed cavity photon $n = 1$, as shown in Fig. 6(a). Figure 6(a) shows the exciton-polariton branches LPB and UPB, the Rabi splittings Ω, and the photon shifts Δ for $N = 25$, corresponding to LPB and UPB in Fig. 5(f). We observe a significant photon shift of $\Delta = 582$ meV at the crossing point $Q_{ex1} = 0.7 \times 10^{-2}$ nm^{-1}. However, the Rabi splitting, the moment when LPB and UPB are the closest, is approximately twice as small, $\Omega = 297$ meV.

Figure 6(b) shows the Rabi splitting Ω (green dots) and photon shift Δ (orange squares) as a function of the number of layers N. The Rabi splitting and the photon shift saturate to $\Omega \sim 350$ meV and to $\Delta = 820$ meV, respectively. For small N the photon shift is still very small, the crossing points with unperturbed and shifted photons are very close [see Fig. 5(b)] so that the Ω is approaching Δ. This allows us to estimate the Rabi splitting for $N = 1$ (when LBP and UPB still overlap) to $\Omega \approx \Delta = 50$ meV. Thus, a transition from weak, $\Omega \sim 50$ meV for $N = 1$, to strong, $\Omega \sim 350$ meV for $N = 60$, exciton-photon coupling, can be noticed. For comparison we also calculate the Rabi splitting Ω_0 when Al_2O_3 substrate is removed but the molecular film is kept at the same place. The substrate removal causes the blueshift of $n = 1$ photon so

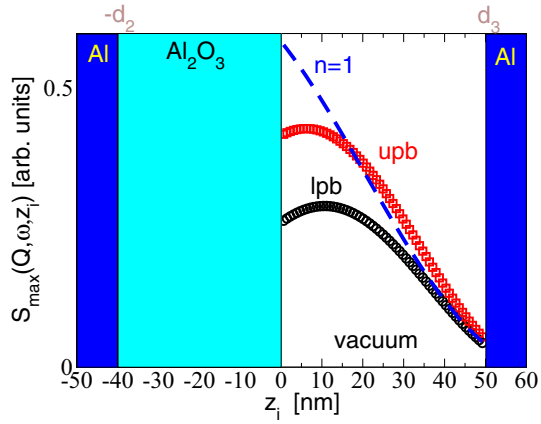

FIG. 7. The maximal intensity $S_{\max}(Q, \omega, z_i)$ of LPB and UPB at Rabi splitting, denoted as lpb (black circles) and upb (red squares), respectively, as a function of C_{60} layer positions, $z_i = z_0, z_0 + c, z_0 + 2c, \ldots, z_0 + 61c$. The maximal intensity of the $n = 1$ cavity-photon in an empty ($N = 0$) cavity (at exciton-photon crossing) is denoted by blue dashed line. The thickness of the C_{60} film is chosen to be $N = 61$ so that the C_{60} film completely fills the vacuum cavity. The lpb and upb maxima are also denoted in Fig. 6(c).

that for $N < 25$ it does not cross the exciton ω_{ex1}. However, for $N \geqslant 25$ the photon is again redshifted below exciton ω_{ex1} and they start to hybridize. The Rabi splitting Ω_0 (magenta circles) is just slightly larger than Rabi splitting Ω which supports earlier conclusions that the substrate weakly affects the binding. More quantitatively, the Rabi splittings Ω and Ω_0 at the saturation point ($N = 61$) are 352 and 401 meV, respectively.

The important contribution of this research is also to clarify the N dependent exciton-photon binding scaling mechanism. If the wavelength of the cavity photon perpendicular to the cavity surface is much larger than the C_{60} slab thickness Nc ($1/|\beta_3| \gg Nc$) the electromagnetic field coherently excites the currents across the C_{60} slab and it effectively behaves as one 2D sheet of effective conductivity $N\tilde{\sigma}(\omega)$. Blue stars in Fig. 6(b) show the Rabi splitting $\Omega_{N\sigma}$ in a single C_{60} sheet of optical conductivity $N\tilde{\sigma}(\omega)$. Indeed, the Rabi splittings $\Omega_{N\sigma}$ and Ω (the Rabi splitting in N spatially separated sheets, each of conductivity $\tilde{\sigma}$) coincide for $N \leqslant 15$. However, if $1/|\beta_3| \approx Nc$ the coherence effect breaks down because the distribution of the induced currents is no longer coherent perpendicular to the C_{60} slab (which will also be demonstrated in Fig. 7) and the photon-polarization coupling becomes less efficient. In Fig. 6(b) this manifests as a faster saturation of Rabi splitting Ω then Rabi splitting $\Omega_{N\sigma}$ for $N > 15$.

Figure 6(c) shows the intensity of the s(TE) electromagnetic modes in the C_{60} film of different thicknesses $N = 5, 10, \ldots, 61$, at the avoided crossing. The $N = 0$ represents the spectral intensity of the unperturbed cavity photon $n = 1$. The two splitted peaks that appear in the spectrum represent exciton-polaritons LPB and UPB, and the distance between them is the Rabi splitting Ω. We notice an increase of Ω and a decrease of exciton-polaritons intensity with N. The decrease of the exciton-polariton intensity in Nth layer is, beside its general decrease in intensity with number N, also due to the spatial distribution of the electromagnetic field through the

TABLE I. The Rabi splittings $\hbar\Omega$ and $\hbar\Omega_0$ of cavity photon $n = 1$ interacting with the excitons ω_{ex1}, ω_{ex2}, and ω_{ex3} in the C_{60} film of thickness $N = 61$ and the Rabi splittings $\hbar\Omega_{\text{hBN}}$ of the cavity photon $n = 1$ interacting with the the hBN exciton ω_{hBN} in the hBN monolayer ($N = 1$) and in the hBN multilayer ($N = 21$). The last column summarizes the experimental Rabi splittings in dye molecule microcavities, for comparison. The energies are in meV.

	$\omega_{\text{ex1}}/\omega_{\text{hBN}}$	ω_{ex2}	ω_{ex3}	Expt. (Dye)
$\hbar\Omega$	352	570	820	430 [33]
$\hbar\Omega_0$	401	600	820	450 [34]
$\hbar\Omega_{\text{hBN}}$ (1 ML)	207			700 [35]
$\hbar\Omega_{\text{hBN}}$ (21 ML)	830			1120 [36]

C_{60} film. Namely, the electrical field of the exciton-polariton qualitatively follows the electrical field of the unperturbed cavity mode $n = 1$, so the intensity of the exciton-polariton in the Nth layer will decrease how the Nth layer approaches the metallic surface (where the electrical field is expected to rapidly drop to zero). This is clearly illustrated in Fig. 7 showing the maximal intensity

$$S_{\max}(Q, \omega, z_i) = -\text{Re}\, \mathcal{E}^{ii}_{xx}(Q_y \mathbf{y}, \omega)$$

of LPB and UPB at Rabi splitting, denoted as "lpb" (black circles) and "upb" (red squares), as a function of C_{60} layer positions $z_i = z_0, z_0 + c, z_0 + 2c, \ldots, z_0 + 61c$. The thickness of the C_{60} film is chosen to be $N = 61$ so that the C_{60} film completely fills the vacuum region ($0 < z < d_3$). The lpb and upb maxima are also denoted in Fig. 6(c). The blue dashed line shows the intensity of the unperturbed $n = 1$ cavity mode at the exciton-photon crossing point ($Q = 0.07$ nm^{-1}, $\omega_{\text{ex1}} = 3.9$ eV). It can be clearly seen that the intensity of LPB and UPB decrease as z_i approaches the metallic surface, while they have maxima approximately in the middle of the entire metallic cavity.

Further enhancement of the photon-exciton binding can be achieved by using molecules that support highly intensive excitons. The last column in Table I summarizes the experimental data of the exciton-polaritons Rabi splitting in the various dye molecule thin films placed in the cavity devices [33–36]. Considering that the dye molecules absorb in the visible frequency range (<2 eV) this Rabi splitting, which is between 50% and 100% of the exciton energy, can be characterized as a giant or ultrastrong light-molecule coupling. In our case, the ω_{ex1} exciton-photon splitting is ~10% of exciton energy which belongs to the strong binding regime. Still, the splitting of more intensive excitons ω_{ex2} and ω_{ex3} should be larger. Columns 2–4 in Table I summarize the Rabi splittings Ω and Ω_0 of three excitons ω_{ex1}, ω_{ex2}, and ω_{ex3}, where the thickness of the C_{60} film is chosen to be $N = 61$, when the binding is saturated. The splitting of ω_{ex2} exciton is ~12%, while, the splitting of the ω_{ex3} exciton is even ~14% of the exciton energy which can be, due to criteria $\Omega/\omega_{\text{ex}}, \Omega/\omega_n >$ 10% [38], characterized as ultrastrong coupling.

Finally, the proposed formulation can be easily extended to calculate the exciton-photon binding in the heterostructures of 2D crystals such as TMDs or hBN. In that case, instead of molecular surface optical conductivity $\tilde{\sigma}$ in the

Dyson's equation (4), the 2D optical conductivity σ should be included [12,30]. For comparison, here we calculate the exciton-polariton splitting in the hBN monolayer ($N = 1$) and in an artificial hBN heterostructure composed of $N = 21$ hBN layers, where we use the hBN single-layer optical conductivity σ derived in Ref. [30]. The cavity parameters z_0, c, d_2, and d_3 are kept the same as in the case of the C_{60} cavity. The calculated Rabi splittings are 207 meV for $N = 1$ and ~830 meV for $N = 21$ (as also listed in the third and fourth rows of Table I), which is 3.5% and 14% of the hBN exciton energy $\omega_{ex} \sim 6$ eV, respectively. These results clearly demonstrate that exciton-photon binding can be enhanced not only by choosing the material with large exciton oscillatory strength but also (more radically) by increasing the number of crystal layers N in the van der Waals heterostructures.

IV. CONCLUSIONS

We theoretically simulate the transition from weak to strong and ultrastrong exciton-photon binding in the van der Waals layered molecular crystals by increasing the number of crystal layers N. In particular, we investigate the coupling between cavity photon and excitons of the C_{60} films by using recently proposed *ab initio* quantum-electrodynamical Bethe-Salpeter equations. The Rabi splittings quantitatively agree with the recent experimental results on organic molecular crystals. The theory is also applied to estimate the exciton-photon binding in heterostructures of 2D crystals. Exciton-photon binding enhancements of factors 7 and 4 are achieved in the C_{60} and hBN multilayers, respectively. These results imply that just a few nanometer thick 2D van der Waals heterostructures are capable to significantly modify the cavity photon zero-point fluctuation energy and thus cause strong Casimir attraction. In other words, the cavity tends to "collapse" the van der Waals crystal into itself. Another fundamental implication is manifestation of the "ghost mode," the coexistence of the electron-hole pair and transverse s(TE) photon providing the collective transversal polarization modes that has no analog in the nonretarded limit ($c \to \infty$). In contrast to the p(TM) plasmon-polariton, which in the nonretarded limit collapses into longitudinal plasmon, the s(TE) exciton-polariton in the same limit vanishes. Therefore, the layered van der Waals heterostructures support the electron-hole-photon entangled polarization mode which oscillates perpendicular to its direction of propagation. The tunability of electromagnetic properties (in energy and spatial domain) by changing the thickness of the heterostructure for only a few nanometers is potentially applicable in optoelectronics as waveguides or optical cables or in chemical and biological sensing. Finally, present consideration might be helpful in addressing the cavity-induced structural phase transitions [73,74] and charge density waves [75], once the lattice degrees of freedom are included and the photon-phonon-electron problem is treated self-consistently.

ACKNOWLEDGMENTS

The authors acknowledge financial support from the Croatian Science Foundation (Grant No. IP-2020-02-5556) as well as from the European Regional Development Fund for the "QuantiXLie Centre of Excellence" (Grant KK.01.1.1.01.0004). Computational resources were provided by the Donostia International Physic Center (DIPC) computing center.

[1] D. N. Basov, A. Asenjo-Garcia, P. James Schuck, X. Zhu, and A. Rubio, Nanophotonics **10**, 549 (2021).
[2] E. A. Vinogradov, Phys. Rep. **217**, 159 (1992).
[3] J. M. Pitarke, V. M. Silkin, E. V. Chulkov, and P. M. Echenique, Rep. Prog. Phys. **70**, 1 (2007).
[4] Y. Xu, L. Wu, and L. K. Ang, Phys. Rev. Appl. **12**, 024029 (2019).
[5] V. M. Harutunian, H. L. Margarian, V. A. Melicksetian, and J. R. Panossian, J. Phys.: Condens. Matter **1**, 847 (1989).
[6] D. T. Ha, D. T. Thuy, V. T. Hoa, T. T. Thanh Van, and N. Ai Viet, J. Phys.: Conf. Ser. **865**, 012007 (2017).
[7] H. Zhang, B. Abhiraman, Q. Zhang, J. Miao, K. Jo, S. Roccasecca, M. W. Knight, A. R. Davoyan, and D. Jariwala, Nat. Commun. **11**, 3552 (2020).
[8] P. Kumar, J. Lynch, B. Song, H. Ling, F. Barrera, K. Kisslinger, H. Zhang, S. B. Anantharaman, J. Digani, H. Zhu, T. H. Choudhury, C. Mc Aleese, X. Wang, B. R. Conran, O. Whear, M. J. Motala, M. Snure, C. Muratore, J. M. Redwing, N. R. Glavin, E. A. Stach *et al.*, Nat. Nanotechnol. **17**, 182 (2022).
[9] S. B. Anantharaman, C. E. Stevens, J. Lynch, B. Song, J. Hou, H. Zhang, K. Jo, P. Kumar, J.-C. Blancon, A. D. Mohite, J. R. Hendrickson, and D. Jariwala, Nano Lett. **21**, 6245 (2021).
[10] S. B. Anantharaman, K. Jo, and D. Jariwala, ACS Nano **15**, 12628 (2021).
[11] D. Jariwala, A. R. Davoyan, G. Tagliabue, M. C. Sherrott, J. Wong, and H. A. Atwater, Nano Lett. **16**, 5482 (2016).
[12] D. Novko, K. Lyon, D. J. Mowbray, and V. Despoja, Phys. Rev. B **104**, 115421 (2021).
[13] V. Despoja and L. Marusic, Int. J. Mol. Sci. **23**, 6943 (2022).
[14] T. Low, A. Chaves, J. D. Caldwell, A. Kumar, N. X. Fang, P. Avouris, T. F. Heinz, F. Guinea, L. Martin-Moreno, and F. Koppens, Nat. Mater. **16**, 182 (2017).
[15] A. Ramasubramaniam, Phys. Rev. B **86**, 115409 (2012).
[16] Y. Li, A. Chernikov, X. Zhang, A. Rigosi, H. M. Hill, A. M. van der Zande, D. A. Chenet, E.-M. Shih, J. Hone, and T. F. Heinz, Phys. Rev. B **90**, 205422 (2014).
[17] D. Y. Qiu, F. H. daJornada, and S. G. Louie, Phys. Rev. Lett. **111**, 216805 (2013).
[18] Y. Lin, X. Ling, L. Yu, S. Huang, A. L. Hsu, Y.-H. Lee, J. Kong, M. S. Dresselhaus, and T. Palacios, Nano Lett. **14**, 5569 (2014).
[19] J. Yan, K. W. Jacobsen, and K. S. Thygesen, Phys. Rev. B **86**, 045208 (2012).
[20] F. Ferreira and R. M. Ribeiro, Phys. Rev. B **96**, 115431 (2017).
[21] C. E. P. Villegas, A. S. Rodin, A. C. Carvalho, and A. R. Rocha, Phys. Chem. Chem. Phys. **18**, 27829 (2016).
[22] X. Wang, A. M. Jones, K. L. Seyler, V. Tran, Y. Jia, H. Zhao, H. Wang, L. Yang, X. Xu, and F. Xia, Nat. Nanotechnol. **10**, 517 (2015).
[23] X. Liu, T. Galfsky, Z. Sun, F. Xia, E.-c. Lin, Y.-H. Lee, S. Kéna-Cohen, and V. M. Menon, Nat. Photonics **9**, 30 (2015).

[24] S. Dufferwiel, S. Schwarz, F. Withers, A. A. P. Trichet, F. Li, M. Sich, O. Del Pozo-Zamudio, C. Clark, A. Nalitov, D. D. Solnyshkov, G. Malpuech, K. S. Novoselov, J. M. Smith, M. S. Skolnick, D. N. Krizhanovskii, and A. I. Tartakovskii, Nat. Commun. **6**, 8579 (2015).

[25] L. C. Flatten, Z. He, D. M. Coles, A. A. P. Trichet, A. W. Powell, R. A. Taylor, J. H. Warner, and J. M. Smith, Sci. Rep. **6**, 33134 (2016).

[26] S. Dufferwiel, T. P. Lyons, D. D. Solnyshkov, A. A. P. Trichet, A. Catanzaro, F. Withers, G. Malpuech, J. M. Smith, K. S. Novoselov, M. S. Skolnick, D. N. Krizhanovskii, and A. I. Tartakovskii, Nat. Commun. **9**, 4797 (2018).

[27] J. Gu, J. Gu, L. Waldecker, D. Rhodes, A. Raja, J. C. Hone, T. F. Heinz, S. Kéna-Cohen, T. Pohl, and V. M. Menon, Nat. Commun. **12**, 2269 (2021).

[28] M. Förg, L. Colombier, R. K. Patel, J. Lindlau, A. D. Mohite, H. Yamaguchi, M. M. Glazov, D. Hunger, and A. Högele, Nat. Commun. **10**, 3697 (2019).

[29] Z. Fei, M. E. Scott, D. J. Gosztola, J. J. Foley IV, J. Yan, D. G. Mandrus, H. Wen, P. Zhou, D. W. Zhang, Y. Sun, J. R. Guest, S. K. Gray, W. Bao, G. P. Wiederrecht, and X. Xu, Phys. Rev. B **94**, 081402(R) (2016).

[30] D. Novko and V. Despoja, Phys. Rev. Res. **3**, L032056 (2021).

[31] D. G. Lidzey, D. D. C. Bradley, M. S. Skolnick, T. Virgili, S. Walker, and D. M. Whittaker, Nature (London) **395**, 53 (1998).

[32] P. A. Hobson, W. L. Barnes, D. G. Lidzey, G. A. Gehring, D. M. Whittaker, M. S. Skolnick, and S. Walker, Appl. Phys. Lett. **81**, 3519 (2002).

[33] N. Takada, T. Kamata, and D. D. C. Bradley, Appl. Phys. Lett. **82**, 1812 (2003).

[34] S. Kena-Cohen and S. R. Forrest, Phys. Rev. B **77**, 073205 (2008).

[35] T. Schwartz, J. A. Hutchison, C. Genet, and T. W. Ebbesen, Phys. Rev. Lett. **106**, 196405 (2011).

[36] S. Gambino, M. Mazzeo, A. Genco, O. Di Stefano, S. Savasta, S. Patane, D. Ballarini, F. Mangione, G. Lerario, D. Sanvitto, and G. Gigli, ACS Photonics **1**, 1042 (2014).

[37] S. Kena-Cohen, S. A. Maier, and D. D. C. Bradley, Adv. Opt. Mater. **1**, 827 (2013).

[38] R. F. Ribeiro, L. A. Martinez-Martinez, M. Du, J. Campos-Gonzalez-Angulo, and J. Yuen-Zhou, Chem. Sci. **9**, 6325 (2018).

[39] L. A. Martínez-Martínez, R. F. Ribeiro, J. Campos-González-Angulo, and J. Yuen-Zhou, ACS Photonics **5**, 167 (2018).

[40] T. S. Haugland, E. Ronca, E. F. Kjonstad, A. Rubio, and H. Koch, Phys. Rev. X **10**, 041043 (2020).

[41] S. Latini, E. Ronca, U. De Giovannini, H. Hubener, and A. Rubio, Nano Lett. **19**, 3473 (2019).

[42] V. Despoja, I. Lončarić, D. J. Mowbray, and L. Marušić, Phys. Rev. B **88**, 235437 (2013).

[43] M. S. Tomaš, Phys. Rev. A **51**, 2545 (1995).

[44] V. Despoja, M. Šunjić, and L. Marušić, Phys. Rev. B **80**, 075410 (2009).

[45] O. Amelines-Sarria, P. C. dos Santos Claro, P. L. Schilardi, B. Blum, A. Rubert, G. Benitez, V. A. Basiuk, A. G. Orive, A. H. Creus, C. Díaz, and R. C. Salvarezza, Org. Electron. **12**, 1483 (2011).

[46] C. Elschner, A. A. Levin, L. Wilde, J. Grenzer, C. Schroer, K. Leo, and M. Riede, J. Appl. Crystallogr. **44**, 983 (2011).

[47] D. Elsenbeck, S. K. Das, and L. Velarde, Phys. Chem. Chem. Phys. **19**, 18519 (2017).

[48] A. Huttner, T. Breuer, and G. Witte, ACS Appl. Mater. Interfaces **11**, 35177 (2019).

[49] E. Seydel, R. Hoffmann-Vogel, and M. Marz, Nanotechnology **30**, 025703 (2019).

[50] A. I. Oreshkin, R. Z. Bakhtizinb, J. T. Sadowskic, and T. Sakuraid, Bull. Russ. Acad. Sci. Phys. **73**, 883 (2009).

[51] S. Bommel, N. Kleppmann, C. Weber, H. Spranger, P. Schafer, J. Novak, S. V. Roth, F. Schreiber, S. H. L. Klapp, and S. Kowarik, Nat. Commun. **5**, 5388 (2014).

[52] Y. M. Acevedo, R. A. Cantrell, P. G. Berard, D. L. Koch, and P. Clancy, Langmuir **32**, 3045 (2016).

[53] W. Janke and T. Speck, Phys. Rev. B **101**, 125427 (2020).

[54] L. Chen, X. Wang, and S. Kumar, Sci. Rep. **5**, 12763 (2015).

[55] C. A. Rozzi, D. Varsano, A. Marini, E. K. U. Gross, and A. Rubio, Phys. Rev. B **73**, 205119 (2006).

[56] D. Novko, M. Šunjić and V. Despoja, Phys. Rev. B **93**, 125413 (2016).

[57] P. Giannozzi, S. Baroni, N. Bonini, M. Calandra, R. Car, C. Cavazzoni, D. Ceresoli, G. L. Chiarotti, M. Cococcioni, I. Dabo *et al.*, J. Phys.: Condens. Matter **21**, 395502 (2009).

[58] N. Troullier and J. L. Martins, Phys. Rev. B **43**, 1993 (1991).

[59] D. R. Hamann, Phys. Rev. B **88**, 085117 (2013).

[60] J. P. Perdew, K. Burke, and M. Ernzerhof, Phys. Rev. Lett. **77**, 3865 (1996).

[61] J. H. Weaver, J. Martins, T. Komeda, Y. Chen, T. R. Ohno, G. H. Kroll, N. Troullier, R. E. Haufler, and R. E. Smalley, Phys. Rev. Lett. **66**, 1741 (1991).

[62] R. W. Lof, M. A. van Veenendaal, B. Koopmans, H. T. Jonkman, and G. A. Sawatzky, Phys. Rev. Lett. **68**, 3924 (1992).

[63] J. D. Sau, J. B. Neaton, H. J. Choi, S. G. Louie, and M. L. Cohen, Phys. Rev. Lett. **101**, 026804 (2008).

[64] X. Blase, C. Attaccalite, and V. Olevano, Phys. Rev. B **83**, 115103 (2011).

[65] V. Despoja, L. Basioli, J. S. Parramon, and M. Mičetić, Sci. Rep. **10**, 65 (2020).

[66] J. Berkowitz, J. Chem. Phys. **111**, 1446 (1999).

[67] B. V. Lobanov and A. I. Murzashev, Russ. Phys. J. **59**, 856 (2016).

[68] M. L. Tiago, P. R. C. Kent, R. Q. Hood, and F. A. Reboredo, J. Chem. Phys. **129**, 084311 (2008).

[69] V. V. Shnitov, V. M. Mikoushkin, and Y. S. Gordeev, Microelectron. Eng. **69**, 429 (2003).

[70] V. V. Shnitov and V. M. Mikoushkin, Fuller. Nanotub. Carbon Nanostr. **20**, 324 (2012).

[71] V. Despoja and D. J. Mowbray, Phys. Rev. B **89**, 195433 (2014).

[72] V. Despoja and L. Marušić, J. Phys.: Condens. Matter **26**, 485012 (2014).

[73] S. Latini, D. Shin, S. A. Sato, C. Schäfer, U. De Giovannini, H. Hübener, and A. Rubio, Proc. Natl. Acad. Sci. USA **118**, e2105618118 (2021).

[74] Y. Ashida, A. Imamoglu, J. Faist, D. Jaksch, A. Cavalleri, and E. Demler, Phys. Rev. X **10**, 041027 (2020).

[75] G. Jarc, S. Y. Mathengattil, A. Montanaro, F. Giusti, E. M. Rigoni, F. Fassioli, S. Winnerl, S. Dal Zilio, D. Mihailovic, P. Prelovšek, M. Eckstein, and D. Fausti, arXiv:2210.02346.